On the role of density-driven dissolution of CO_2 in phreatic karst systems

H. Class[1], P. Bürkle [1], T. Sauerborn [1], O. Trötschler [1], B. Strauch [2], M. Zimmer [2]

[1]Institute for Modelling Hydraulic and Environmental Systems, University of Stuttgart, Germany
[1]GFZ German Research Centre for Geosciences, Potsdam, Germany

Key Points:

- Density-driven CO_2 dissolution is a process that deserves more attention in karstification theories and beyond.
- Fluctuating CO_2 partial pressures in the vadose zone can enhance dissolution of CO_2 in phreatic karst water.
- Generic scenarios are used to demonstrate how density-driven dissolution can contribute to replenishing CO_2 in karst water.

Corresponding author: H. Class, holger.class@iws.uni-stuttgart.de

Abstract

Density-driven dissolution of carbon dioxide in water is a well-known and much described mechanism in geological sequestration of this greenhouse gas. It is remarkable that such enhanced dissolution does not receive much attention in karst hydrology and speleology.

Models and hypotheses on karst development are complex and consider many different processes. We focus here on the influence of CO_2 partial gas pressures at the interface between atmosphere and karst water on the dynamics of dissolved CO_2 concentrations below the water table. Seasonal variation of microbial soil activity and root respiration or barometric-pressure changes cause fluctuations in CO_2 partial pressures. Dependent on the existence and strength of a karst-water background flow, fingering regimes might be triggered causing enhanced dissolution of CO_2 This allows replenishment of CO_2, and, thus, dissolutional power even deep in the water body without the need for percolating water to transport dissolved CO_2.

We present and discuss simplified and generic experimental and computational scenarios to strengthen our claim, and we try to give answers to: how much? and under which circumstances? The applied numerical model solves the Navier-Stokes equation with water density dependent on CO_2 concentration and temperature. We show that calculated CO_2 mass fluxes into the water bodies are dependent on the ratio of Péclet to Rayleigh numbers (Pe/Ra) and show a local minimum around Pe/Ra$\approx$1, i.e. when natural and forced convection are about equal.

Concluding, we claim there is sufficient reason to consider density-driven dissolution as a process of relevance in karstification if circumstances are given.

Plain Language Summary

Karst systems in limestones form in rock that is soluble in the presence of water charged with carbonic acid. The required carbon dioxide (CO_2) can take different pathways to replenish dissolutional power in karst water. This study discusses a pathway that did not receive much attention yet.

The density of water increases when CO_2 dissolves, and, when dissolution occurs at the water table, instabilities may be induced. This can trigger fingering-like flow and enhance the rate of dissolution at the water table. The phenomenon is well-known as a major trapping mechanism for CO_2 injected into geological formations for mitigating greenhouse-gas emissions. The more so is it remarkable that the same phenomenon is not discussed in karst hydrology and speleology. Of course, the different conditions of concentrations, pressures, and temperatures require attention. For realistic conditions, we demonstrate experimentally and by numerical simulations that density-induced transport of CO_2 is significant. The lab experiment used a 6 m long vertical column and imitates an analog to a cave lake. We can see that within a few months time, significant amounts of CO_2 can be dissolved at karst-typical elevated gaseous CO_2 concentrations. The influence of natural ground-/karst water background flow is addressed by numerical simulations.

1 Introduction

Karst systems are found in many regions around the world. In the order of 10 % of the continental surface is karst (Ford & Williams, 2007; Mangin, 1975). Karst is incredibly complex and manifold, and the processes that dominate karstification strongly depend on the hydrological and geomorphological properties of the karstic systems, which are subject to constant change while karstification is ongoing. The word 'karst' has its etymological origin in the German language in the description of decalcified mountaineous regions (Kluge, 2012). It might have found its way into the German language from the Karst Plateau in the Dinarides (Bakalowicz, 2005; Stevanovic, 2015; Mangin, 1975), a strongly karstified mountain range in former Yugoslavia. Essentially, karstification hap-

pens in soluble rocks in contact with water, typically at the earth's surface or close to it. Karst research has evident relations to the disciplines and sub-disciplines of hydrology, geology, speleology, geomorphology, hydrogeology, etc. Karstic rocks are typically carbonate rocks made of Calcium and Magnesium minerals, where limestone ($CaCO_3$) and dolomite ($CaMg[CO_3]_2$) are the most important types. During karstification, these rocks are eroded mechanically, and, more importantly, corroded chemically. The corrosion of calcite and dolomite is driven by the availability of dissolved CO_2 in the water.

Where does the CO_2 come from and what are its migration pathways into karst water? Textbooks on karst research and a multitude of papers generally agree that CO_2 is produced and accumulated by seasonally fluctuating biological activity and root respiration in the vadose zone, e.g., (Dreybrodt, 1988; Bonacci, 1987; Ford & Williams, 2007; Stevanovic, 2015; White, 2018; Klimchouk et al., 2000). The vadose zone is also denoted as the saturated zone, or, in the karst context, we could refer to it as epikarst. There, the CO_2 is dissolved by percolating meteoric water, and a hydraulic gradient is then required to transport water through the rock, where the aggressiveness of the CO_2-enriched water has a potential to dissolve carbonate. Flow and transport are crucially important, since the dissolved Ca^{2+} and carbonate ions will affect the reaction kinetics and the dissolution reaction will level out if the reaction products are not transported away. While we do not discuss hypogenic karst systems here, it is generally accepted that in epigenic systems, the CO_2 has its origin in the epikarst above the karst-water table and requires downward transport to corrode carbonate rocks (Audra & Palmer, 2011; Spötl et al., 2016; Kaufmann et al., 2014; Bakalowicz, 2005; Klimchouk et al., 2000; Houillon et al., 2020).

Consequently, one should expect more corrosion at or close to the surface rather than deep inside the rock. An approach to explain corrosion deep inside employs mixing corrosion (or mixing dissolution) (Bögli, 1980). Two water flows, which can be both in a state of calco-carbonic equilibrium, always form a calcite-aggressive solution when they mix, for example, in joints. Another approach explains dissolution of calcite deep inside the rock with non-linear dissolution kinetics that allow for the water to keep some remaining dissolutional power while penetrating deep into the rock, e.g., (Gabrovšek & Dreybrodt, 2000; Ford & Ewers, 1978; Dreybrodt, 2004; Kaufmann et al., 2014).

1.1 The case for density-driven dissolution as a mechanism to replenish CO_2 in karst water

This study investigates yet another mechanism to replenish CO_2 in epiphreatic karst water. We try to make a case for a well-known process that is so far not thoroughly discussed in the karst-specific literature: density-driven dissolution. This can contribute to closing gaps in explanations or to adding physically based insights to speculative comments on CO_2 dynamics in some literature.

It is important to distinguish an open system from a closed system. In open karst systems, gaseous CO_2 remains in contact with the water and allows for replenishment until an equilibrium between solid (carbonates), liquid water, and gas is achieved. In contrast, in a closed system, where there is no replenishment of CO_2, the final state of equilibrium is an internal one between the dissolved species. (Atkinson, 1977) suggests accordingly, that higher carbonate hardness of water indicates a tendency towards an open system. He further relates fluctuations and mean values of CO_2 soil concentrations with spring waters, which show often corresponding oscillations in $p_{CO_2,eq}$, the calculated partial pressures in assumed equilibrium. Larger groundwater bodies may dampen this in spring waters where the $p_{CO_2,eq}$ is rather constant. (Atkinson, 1977), Fig. 4, compares the detected hardness at springs with hardness of soil water and potential hardness calculated on the basis of assuming the above-mentioned equilibrium in an open system. The detected hardness in spring water is much higher than the hardness of soil water. The potential hardness of soil water approaches the detected hardness, in summer months

even exceeds it. Interestingly, the author concludes that the discrepancy must be made from another source of CO_2 in the air of the zone where water percolates. Our reasoning, however, is that this might well be the case, but we don't necessarily need to have the percolating water in contact with these high air concentrations. It can be sufficient or even be more effective to have these high CO_2 partial pressures at the karst water table where they trigger density-induced dissolution.

(Audra & Palmer, 2011) write on controls of epigenic caves, they discuss the different hydrologic zones in karst and highlight the importance of the epiphreatic zone where water-table fluctuations take place. Not all epiphreatic water may be connected, and local ponding due to local geologic features might occur. In the early history of a cave, water circulation is rather very small since no good networks exist yet, there is low permeability, and water is nearly saturated with dissolved calcite. Later on, under hydraulic gradients, larger fluxes, even turbulence may occur. One may object, what if we have intermittent regimes, with periods where no or only very small hydraulic gradients exist? In such cases, density-driven dissolution may make a difference. (Audra & Palmer, 2011) further give an interesting review of earlier and current conceptual ideas which do not necessarily exclude each other, since nature is enormously manifold, and there might be many mechanisms adding to the overall picture.

In his textbook, (Dreybrodt, 1988) explains that circulation of water controls the development of karst. A free surface of the karst water, and, thus, an interface between the vadose zone and the saturated zone exists only at a later stage of karstification, when fissures or conduits have already developed. According to (Dreybrodt, 1988), the process of karstification starts when a hydraulic gradient is acting in an interconnected system of primary, micro-size fissures of several 10 μ, upon which chemically aggressive groundwater dissolves the rock along these flow paths. This process is self-enhancing since resistance to flow is reduced with increasing channel dimensions. Similar reasoning is found, e.g., in (Mangin, 1975; Mohammadi et al., 2007; Ford & Ewers, 1978). Circulation facilitates corrosion and vice versa, without circulation corrosion quickly stops. But what if water is not flowing? Or circulating intermittently, or only at very small velocities? Is the reaction system then approaching a state of equilibrium? If CO_2 can sink into water bodies and replenish by enhanced dissolution, the process of karstification could go on also without percolating water and it may be sufficient that the reaction products are transported away from time to time. This might contribute to discussions on the role of mixing corrosion, which is described, e.g., by (Bögli, 1980), and which was questioned and put into perspective by (Gabrovšek & Dreybrodt, 2000; Dreybrodt, 2004). The apparent phenomenon of carbonate dissolution even deep inside a rock can be explained by the mixing of different water streams, which always renders the mixed water calcite-aggressive. (Gabrovšek & Dreybrodt, 2000) show in a numerical study that non-linear dissolution models can as well describe dissolution deep inside the rock, however still relying on percolating water in fissures or bedding planes. Consequently, we consider that replenishment of CO_2 by density-driven dissolution during periods of small or no percolation is yet another possible explanation.

Very close to our conceptual idea is the study of (Gulley et al., 2014). They show that CO_2 in the vadose gas, and in particular fluctuations in the partial pressure of CO_2 due to seasonal accumulation, can drive dissolution of carbonates more efficiently than mixing corrosion can explain. Still, they do not mention the mechanism of density-driven dissolution, but simply assume that dissolved CO_2 is evenly distributed throughout the upper 0.5 m of groundwater. (Houillon et al., 2020) discuss the CO_2 dynamics in the atmosphere-soil-epikarst system and its impact on the karstification potential of water. They highlight the mechanisms responsible for higher CO_2 partial pressure in water than in soil, where the soil is the region of production of CO_2.

In their review article, (Ben-Noah & Friedman, 2018) discuss effects of soil aeration and they state that natural aeration is diffusive and to some extent also advective

due to barometric-pressure fluctuations. They present a model for barometric pumping and briefly address also other mechanisms causing advective gas exchange, such as temperature-driven or Venturi-suction due to the Bernoulli-effect resulting from lower pressures in high-velocity wind flow. A multi-year measurement campaign by (Houillon et al., 2020) provided weather data (atmospheric pressure, temperature, rain events), p_{CO_2} in soil, bicarbonate concentration measured in drip water, and $p_{CO_2,eq}$ in (assumed) equilibrium determined with a CO_2-SIc relationship (Peyraube et al., 2015). Soil $p_{CO_2,eq}$, as expected, showed seasonal variation with strong biogenic production in spring and lower production during autumn and winter. They also measured soil CO_2 efflux, which was, again as expected, higher in summer than in winter. But interestingly, it varied strongly with soil moisture. Dry soil correlates with high CO_2 efflux, wet soil (after rain events) with low efflux. Soil moisture and temperature clearly act as an important control for vertical transport of CO_2 in the epikarst. Applying this to our considerations, we see that the seasonally fluctuating CO_2 partial pressures are well studied and understood. But the mechanisms of dissolution still lack some explanations, and density-driven dissolution is not discussed.

Typically, vertical upward ventilation in cold periods transports fresh air into the cave system and dilutes the air, while downward transport in warm periods enriches the cave's air with CO_2. (Kukuljan et al., 2021) conducted a comprehensive study on CO_2 dynamics in a karst system in Slovenia related to microclimatic observations and showed that this typical behavior due to the so-called chimney effect can be superimposed by wind gusts. This leads to extremely complex ventilation patterns that constantly enforce dilution and enrichment of cave air, which also depends on the CO_2 concentrations from the respective outside. So, we think there is reason to believe that this has effects at the epiphreatic interface, and, where background flow is absent or small, density-driven dissolution of CO_2 is likely to occur.

An indicator for different climatic controls on conditions in karstification is the fractionation between the stable carbon isotopes ^{13}C and ^{12}C. Plants prefer the lighter isotope and discriminate against ^{13}C (Werth & Kuzyakov, 2010). Therefore, $\delta^{13}C$ data as found, e.g., in speleothems (Fohlmeister et al., 2020; White, 2018) or in karstic spring waters (Lee et al., 2021), can be used to conclude on effects from different vegetation, soil moisture, temperature, or soil respiration. CO_2 concentrations in karst systems typically show significant contributions from vegetation and soil respiration, while the processes affecting respiration and plant growth are extremely complex, also with inhibitory effects when CO_2 concentrations are high (Ben-Noah & Friedman, 2018). It is not easy to make an argument from $\delta^{13}C$ studies for our case for CO_2 dissolution in karst water. The study of (Fohlmeister et al., 2020) on ^{13}C in speleothems found that high $\delta^{13}C$ values correlate with caves in which ventilation is strong. Ventilation facilitates the mixing of atmospheric CO_2 into the soil gas and, thus, increases $\delta^{13}C$. Ventilation is in our context changing partial pressures of CO_2, the hypothesized driving force of density-driven dissolution. The study of (Lee et al., 2021) reports extrem gradients of CO_2 found in karstic springs, where the authors also analyze ^{13}C. The authors were surprised to find strong spatial variability in dissolved CO_2 concentrations and in their $\delta^{13}C$ although all sample sites were in the same region (same climate, same geology). They assume that at sites with relatively high ^{13}C contents, it might be explained by more intense leaching of carbonate rocks (with higher $\delta^{13}C$) due to longer residence time of the water in the system. If however, now also being speculative, this site was a case where conditions for enhanced dissolution were more favorable than in others, the longer residence time might not necessarily be required for explaining the observation.

(Ma et al., 2014) and (Serrano-Ortiz et al., 2010) hypothesize on large subterranean depots for CO_2 in order to contribute to explaining an apparent imbalance between the amounts of CO_2 released from anthropogenic activities and documented terrestrial or oceanic sinks. They use expressions like 'hidden flows' or 'downward CO_2 fluxes which

seem to have nowhere to go' and assume that groundwater acts as a major sink, although not providing details on mechanisms. We consider it possible that density-driven dissolution can be a contribution to this phenomenon.

We can sum this up: CO_2 density-driven dissolution in water finds no appropriate consideration in the karst and soil-science literature. While most certainly it can not fill all the gaps in knowledge and observations that we mentioned above (and many others not mentioned here), we try to make a case here for taking it into account when conditions are favorable. Once this is recognized, it remains to be elaborated what favorable conditions are.

1.2 Density-driven dissolution in geological storage of CO_2

Before we come back to karst, we summarize briefly abundant related knowledge on density-driven dissolution as a mechanism of major importance for safe long-term storage of CO_2 in deep geological reservoirs (IPCC, 2005).

The injection of CO_2 into a geological formation, e.g., a saline aquifer, typically leads to a segregation of the CO_2 and the brine due to buoyancy. Under reservoir conditions, the CO_2 is typically supercritical and its fluid density is often in the order of half the density of the brine. Thus, the CO_2 phase will end up in a stratum underneath a caprock on top of the brine. Over time, CO_2 dissolves in the brine and increases the brine's density, e.g., (Garcia, 2001). The layering is thus instable, and if the driving force for convection can overcome the attenuating process of diffusion, a fingering process is triggered, eventually resulting in an enhanced dissolution and an effective vertical downward transport of CO_2. This effect has already been discussed in early publications in the field of CO_2 geological storage, e.g., (Weir et al., 1996; Lindeberg & Wessel-Berg, 1997), and is denoted also as solubility trapping (IPCC, 2005).

A similar situation was described phenomenologically and mathematically by (Bénard, 1901) and (Lord Rayleigh, 1916) for convective cells forming due to density differences induced by a fluid of lower temperature resting upon a fluid of higher temperature. The dimensionless Rayleigh number is commonly employed to characterize instability. It can be interpreted as the ratio of a characteristic diffusion time to a characteristic convection time. Important factors of influence are the density difference $\Delta\varrho$, the diffusion coefficient D, the fluid's dynamic viscosity μ, and the characteristic spatial dimensions. (Green & Ennis-King, 2018) use in their definition of the Rayleigh number only one, the reservoir depth, as spatial dimension plus the permeability k, which has units m^2 and represents a resistance to convection; they also consider porosity. High Rayleigh numbers are favorable for convection, while diffusion is dominant in low Rayleigh-number regimes. The onset time of a fingering regime and the characteristic wave length in an unstable layering both depend on the Rayleigh number.

On the subject of CO_2 geological storage, many publications are found on (in-)stability analyses and estimates for the time until the onset of fingering or the wave length of the fingering pattern in porous media, e.g., (Ennis-King & Paterson, 2003a, 2003b; Riaz et al., 2006; Hassanzadeh et al., 2005, 2006; Emami-Meybodi et al., 2015), or the scaling with different dimensionless numbers, e.g., (Hassanzadeh et al., 2007). High-resolution numerical studies on Darcy-type models for porous media also show that the spatial length of discretization has to be very small relative to the scale of a typical storage reservoir in order for modellers to resolve onset time and fingering patterns correctly (Riaz et al., 2006; Pau et al., 2010), making grid-converged results on large spatial reservoir scales practically infeasible. Therefore, more pragmatic approaches avoid the resolution of the fingers and employ effective rates, dependent on permeability, density difference as a function of CO_2 concentration and brine salinity, and fluid viscosity (Pau et al., 2010). An overview is given, for example, in the paper of Green and Ennis-King (2018) (Green & Ennis-King, 2018).

Major distinctions to be made between the scenarios in the context of geological CO_2 storage and in the karst context concern (i) the concentrations and partial pressures of CO_2 that cause the density differences in the water phase. In karst, CO_2 partial pressures are much smaller, thus also the corresponding density differences that trigger the instabilities. (ii) On the other hand, the permeability of a reservoir where CO_2 is stored is usually rather small and gives a resistance to instabilities, while we may have highly permeable fissures or larger open subsurface water bodies, where resistance even to small density differences is very small.

(Erfani et al., 2021) show that CO_2 density-driven flow in carbonate aquifers should not be viewed as an isolated processes but rather strongly coupled to geochemical processes that have significant impact on the convection processes. This holds a fortiori in karst aquifers and karstification where the coupling of flow with reaction drives the genesis and growth of conduits or caves on even longer time scales.

1.3 Measuring CO_2 concentrations in the subsurface

CO_2 in water is one of the three components of dissolved inorganic carbon (DIC), present in natural waters. The other two components, bicarbonate (HCO_3^-) and carbonate ion (CO_3^{2-}) constitute the main buffers in most waters and account for alkalinity (acid neutralizing capacity). Free CO_2 is the most dynamic of the constituents of DIC (Cole and Prairie, 2014) and various configurations have been tested for its proper measurement in water. Especially in oceanographic research, well-developed techniques are applied for short-term measurements of the spatial distribution of CO_2 in the aqueous phase, e.g. (Kana et al., 1994; Bell et al., 2007). However, only few experiences in long-term performance, required for continuous monitoring, exist (Cioni et al., 2007; Camilli & Duryea, 2009; Johnson et al., 2010). Methods of measuring dissolved CO_2 in natural waters are either pH-alkalinity titrations or direct CO_2 measurements. The latter avoids uncertainties associated with pH and alkalinity determination in the field and is most suitable for long-term monitoring of CO_2 concentrations. The methods of direct CO_2 measurements require water-gas partitioning which can be realized either actively by using a head-space unit (Pfeiffer et al., 2011) or passively by applying membrane-separation techniques (Zimmer et al., 2011; De Gregorio et al., 2011; Johnson et al., 2010; Strauch et al., 2020). The permeability of gases through polymeric membranes are well constrained (e.g. (Berean et al., 2014; Merkel et al., 2000; Kjeldsen, 1993; Barrer & Chio, 1965; Pinnau & He, 2004; Schultz & Peinemann, 1996; Raharjo et al., 2007) as membrane-based gas-separation technologies are widely used for various processes such as gas purification, carbon capture, and analytical methods. Gas permeation through polymeric membranes is controlled by the solution-diffusion mechanism. First, the gas molecules are absorbed by the membrane surface, the penetrant dissolves at the membrane interface and is in solution equilibrium with its adjoining feed phase (Stern et al., 1987). It follows the diffusion through the polymer matrix and finally the gas molecules evaporate on the other side of the membrane (Javaid, 2005). Hence, the permeability is controlled by absorption and defined by the solubility of specific gases within the membrane and their diffusion through the membrane matrix (Scholes et al., 2009). The overall concept of membrane-based monitoring is the ability of polymer membranes to allow gaseous components to pass through but not to permit liquids. In equilibrium between feed and permeate, the gaseous permeate can then be analyzed using a conventional gas analyzer. For this, the permeated gas sample is usually transported via pump and regulators to the measurement device (e.g. gas mass spectrometer or an infrared gas analyzer). A direct positioning of a membrane-coated sensor at the permanent sampling position directly into the aqueous environment is an improved setup.

1.4 Summarized research questions and outline

We tried to motivate that density-driven dissolution deserves attention in karstification and soil science. We are not aware of literature discussing this process in the mentioned context. Therefore, we elaborate here some very basic scenarios in order to show that indeed there can be relevant mass influx across the air-water interface and, thus, replenishment of water with CO_2. The following research questions primarily guide this study.

- What do we know about CO_2 dynamics in water bodies exposed to fluctuating CO_2 partial pressures at the water table? Can we measure it? And do we have numerical models that are capable of describing these processes? See also in (Class et al., 2020)
- What are the conditions for density-driven dissolution of CO_2 to occur? Are small density differences sufficient to trigger instabilities?
- Can we estimate density-driven CO_2 dissolution rates, for example, in phreatic caves?
- Is density-driven CO_2 dissolution relevant for karst hydrology, geomorphology, or speleology?

The manuscript is organized as follows. Section 2 investigates CO_2 dissolution into stagnant water in a 6 m tall laboratory column, where we introduce a new measurement setup for CO_2 concentrations in the water body. Section 3 presents exemplary scenarios, which are aimed at demonstrating the influence of forced versus natural convection on the occurrence of density-driven dissolution and its relevance for the transfer of CO_2 from the gas phase into water bodies. We conclude with a discussion and an outlook in Section 4.

2 Stagnant water column exposed to elevated CO_2 partial pressures

We filled a laboratory column with tapwater and exposed it to an elevated gaseous CO_2 concentration, roughly 50 times the current atmospheric concentration, thus imitating cave-air conditions. After stripping the water with ambient air, it was initially in equilibrium with atmospheric conditions. Certainly not likely to happen exactly that way in a cave, this setup imitates the case of a cave lake, which quickly received fresh water, and is then exposed to CO_2-rich cave air conditions. Then, we measured the concentration of dissolved CO_2 over a time period of 60 days in two different depths in the column. The measured values can be compared to results of numerical simulations, thus allowing for a more substantiated discussion of related uncertainties and the relevance of the conclusions we can draw from this study.

2.1 Experiment: Materials and methods

With the design of the setup, we aimed (i) at providing well-controlled conditions, (ii) at a cooling of the water to subsurface-like, close-to-constant temperatures, and (iii) at defining as possible karst-representative CO_2 concentrations in the gas. Therefore, a 6 m long HDPE column (PE 100 SDR 11) with an outer diameter of 0.25 m (OD 250 mm $\times$ 22.7 mm wall thickness, thermal conductivity 0.38 W/(mK)) was filled with tapwater (Bodenseewasserversorgung, Stuttgart) and stripped with ambient air to initialize a CO_2-concentration in the water in equilibrium to $\approx$ 400 ppm gaseous concentration. Before the influx of CO_2 was started as well as after the experiment, water samples were taken and analyzed, the results are shown in Tab. 1. Aiming at creating a cave-like atmosphere, we chose to define a target value of $x_{CO_2} = 20,000$ ppm $\pm 5,000$ ppm atmospheric CO_2-concentration above the water table at the top of the column, which was sealed from the ambient atmosphere with a 0.35 m long cylindrical head space. The head

Table 1. Water parameters before and after the experiment, obtained from water samples after titration and determination of TC and TOC. (Institute for Sanitary Engineering, Water Quality and Solid Waste Management, personal communication)

	Before	After	
pH	8.16	7.40	
p-value	0.046	0.570	mMol/l
m-value	2.65	2.85	mMol/l
TC	33.9	35.9	mg/l
TOC	2.07	1.53	mg/l
TC - TOC	30.9	34.9	mg/l

space serves as a lid and was separated in two chambers (see Fig 1) using a skimming wall to enforce mixing of the gas in the entire air chamber and to avoid a shortcut of the circulating CO_2-enriched air. At the top of one of the hood's chambers, CO_2 was added at times using a 100 l TEDLAR®-PVF bag filled with CO_2 (99.8% purity, atmospheric pressure), while the gas was pumped out from the top of the other chamber. After feeding the CO_2, a small flow of ≈5 l/min, using an air-membrane pump (KNF N86 KTE), was maintained in the hood across the skimming wall. The process is illustrated in Fig. 1. The gaseous CO_2 concentration was continuously monitored and registered by a CO_2 sensor in the hood. We started with manually inducing the CO_2 when the monitored CO_2 concentration in the gas above the water table decreased to values below 1.5%. Later on, we also used a time clock to trigger intermittent feedings. Results are shown in Fig. 2. The water table was located 10 cm below the skimming wall's edge at a height of 5.55 m from the bottom of the column. For a continuous monitoring of the CO_2 concentration in the water, two sensors were installed below the water surface; the upper one at 1 m below the water level and the lower one at 0.15 m above the ground. The upper one was operated between 1020 hPa - 1080 hPa absolute pressure, the lower sensor was operated between 1460 hPa - 1520 hPa. We used PVC-covered Vaisala GMP252 infrared gas sensors (factory-calibrated 0-20,000 ppm, accuracy ± 1.5%) at both water depths and the same sensor without PVC-covering at atmospheric pressure conditions in the gas above the water table. The water-proof but gas-permeable PVC cover of 1.4 mm thickness has a CO_2 permeability of about 15 barrer (Kjeldsen, 1993) (1 barrer = 7.5006×10^{-18} m^3 s/kg), which allows for a relatively fast establishment of equilibrium between the inner gaseous atmosphere of the sensor and the surrounding aqueous environment. The sensors' response time was determined in a certified check gas with 5,200 ppm CO_2 at 0.1 MPa. After about 1 h exposure time, the equilibrium was established. The sensors require 24 V power which is supplied via a 10 m DC power cable from an external source. Signal wires inside the same cable serve for data transmission to a data-acquisition system (ADL-MX Advanced Datalogger). A self-vulcanization tape (3M) was used for a water-proof sealing of the PVC cover and the cable-to-sensor connection. The Vaisala sensors are supplied by the manufacturer with certificates of calibration. For assessing the accuracy of the measurements subsequent to covering, a linear calibration curve was determined using air and check gases with certified CO_2 concentrations of 3,000 ppm and 5,200 ppm, respectively. For the continuous in-situ measurement of dissolved CO_2, the prepared sensors were vertically lowered with the power cable to their defined positions in different depths of the water column.

The sensors were calibrated by the manufacturer at an atmospheric pressure of 1,013 hPa and a temperature of 25 °C. Therefore, the CO_2-concentration signal provided by the sensors requires correction for temperature and pressure deviation from these conditions. Temperature correction is given in the manufacturer's data sheet with ±0.05 % of read-

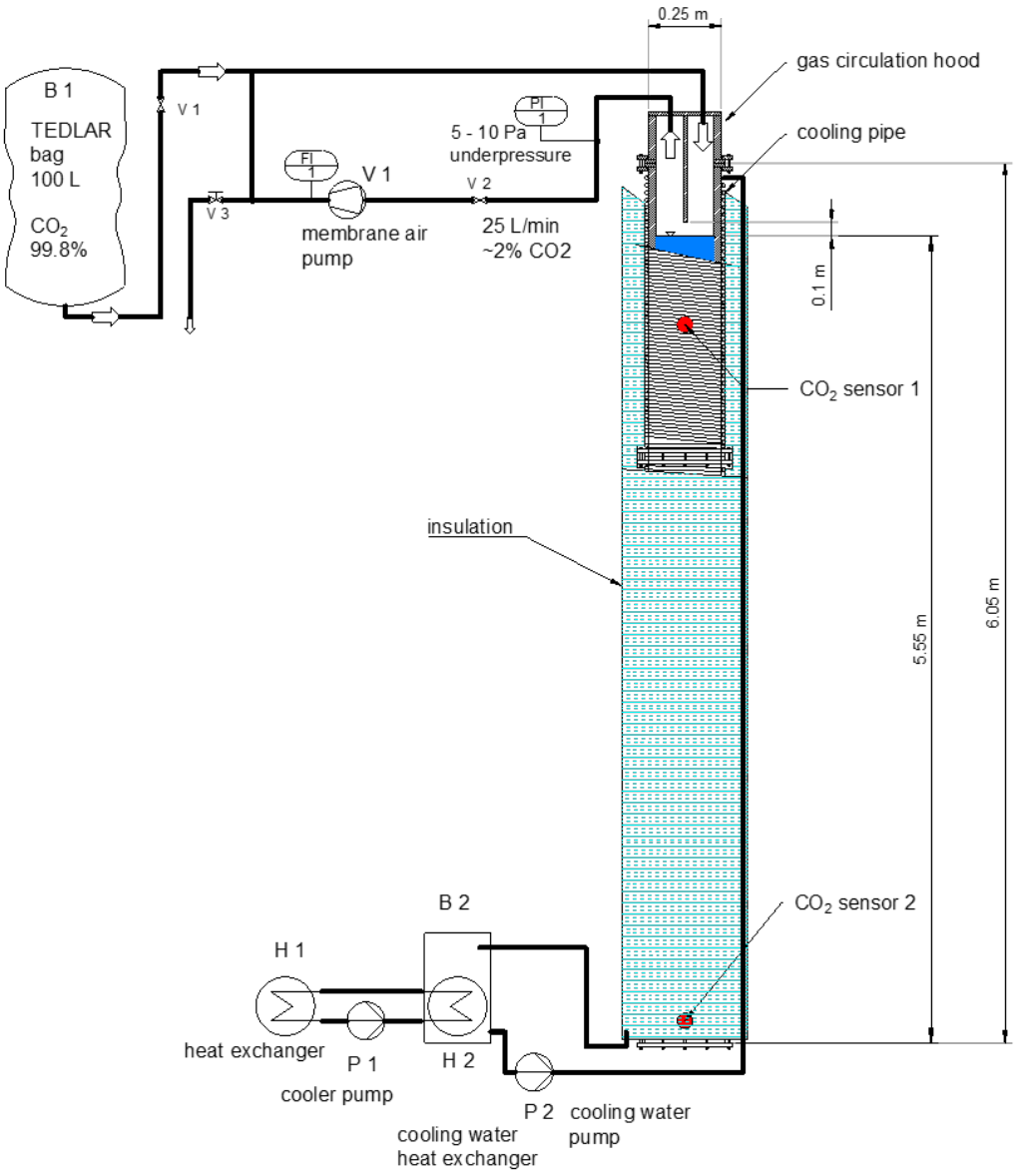

Figure 1. Process diagram of the experimental setup.

ing/°C deviating from the calibration conditions. As in (Johnson et al., 2010), temperatures below calibration conditions require an increase by 0.05 % of reading/°C et vice versa. The pressure correction given by the manufacturer is ±0.015 % of reading/hPa. We note from oral communication with the manufacturer that typically these probes are used at atmospheric conditions, while we apply it at 5.40 m depth. Thus, the deviation from calibration pressure is much higher than for typical atmospheric pressure fluctuations. The manufacturer has then provided us with the following equation for pressure and temperature compensation:

$$c_{\text{corr}} = c_{\text{meas}} \cdot 1,013 \text{ hPa} \cdot (T/(298 \text{ K} \cdot p)). \tag{1}$$

c_{corr} is the corrected and c_{meas} the measured CO_2 concentration of the sensor respectively in ppm or % . T is the temperature in Kelvin and p the pressure in this equation here in hPa during the measurement. In addition, we decided to increase confidence in the pressure correction by producing our own compensation curves and corrections. For this purpose, a measuring pipe was set up which was pressurized with ambient air (≈ 400 ppm) from 0 hPa to 1,000 hPa overpressure. The results of these measurements can be seen in Fig. B1. The deviations at operating pressure of the in-situ sensors can now be taken to calculate a correction factor, which is 0.1240 for the sensor at 1 m below water surface and 0.4181 for the sensor at 0.15 m from the bottom. We use this correction factor with the temperature correction (±0.05 % of reading/°C) mentioned at the beginning of this paragraph. As will be shown later on, our own compensation factors match very well with Eq. (1).

For evaluating how the total CO_2-entry rate into the water, $J_{in}^{CO_2}$, relates to a hypothetical purely diffusive rate (in the absence of density effects), we use the dimensionless Sherwood number (Sh). Sh is accordingly defined here as

$$\text{Sh} = \frac{J_{in}^{CO_2} H}{D \Delta \varrho} \ . \tag{2}$$

We evaluated $J_{in}^{CO_2}$ from the numerical simulations, see Sec. 2.3. $H = 5.55$ m, the height of the water body (see Fig. 1), is used as the characteristic length scale. D is the diffusion coefficient, where we use the same value of $D = 2{\times}10^{-9}$ m^2/s as in (Class et al., 2020). $\Delta\varrho$ is the density difference due to dissolved CO_2 concentrations with densities calculated by using Eq. (A5) at 10 °C. We calculated $\Delta\varrho$ by inserting the concentrations at the water table as the upper value, and for the lower value, we used the CO_2 concentration at 0.15 m from the bottom, corresponding to the position of the lower sensor. The calculations for the Sherwood number are also shown in the DaRUS dataset related to this article (Bürkle et al., 2021).

For maintaining a constant and defined water temperature, the column was insulated (Rockwool panel, 90 mm thickness, aluminium coated, heat conductivity 0.035 W/(mK)) and continuously cooled to 10 °C. A circulation cooler (Lauda WK 1200, 1.2 kW cooling power) permanently provided a 10 °C cold water flow in a 100 m long cooling pipe (Georg Fischer, JRG Sanipex MT, 26 mm OD × 20 mm ID, thermal conductivity 0.43 W/(mK)) that was spiral-wrapped around the column. The cooling system's sufficient capacity can be explained with a few considerations. The heat flux Q through the cooling-water pipe, the wall of the column, and the insulation can be estimated as

$$Q = \lambda \frac{2\pi l}{\ln(r_o) - \ln(r_i)} (T_i - T_o) \ , \tag{3}$$

with λ representing the materials' heat conductivity, l the height of the column, r_i, r_o the inner and outer radius of the column, and T_i, T_o the inner and outer temperatures. The heat flow through the insulation is then obtained as ≈ 31 W for $T_i = 10$ °C in the pipe and $T_o = 25$ °C ambient temperature. The theoretical heat-transfer capacity of the cooling pipe of $l = 100$ m length is ≈ 13.4 kW. The heat transfer through the walls

of the column is calculated to be 357 W. The circulation cooler provides a heat flux of 1.2 kW in maximum. The heat transfer is limited by the heat flux through the walls of the column. The cooler is safely operated at ≈ 20% of its capacity. The installation is illustrated in Fig. 1.

2.2 Experiment: Results

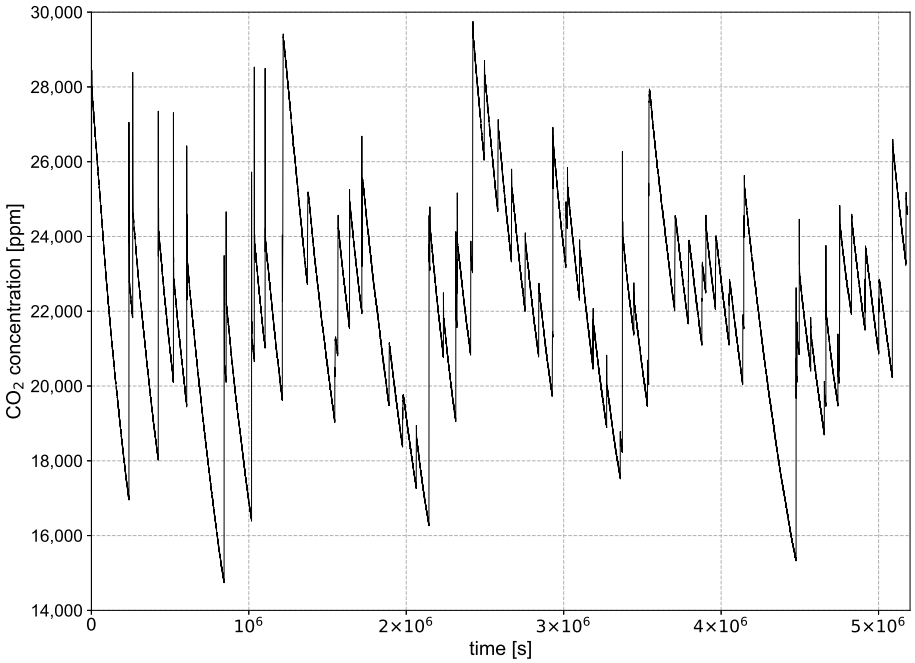

Figure 2. CO_2 concentration in air over time in the head space of the column.

Figure 2 provides the continuously monitored, and already corrected CO_2 concentration (ppm) in the gas phase in the head of the column. As explained above, the fluctuations are a result of the intermittent additions of CO_2 into the head space. Realistic cave-air conditions also show fluctuations, but we did not attempt to imitate representative cave-air fluctuations. The aim was simply to provide a characteristic average concentration of about 20,000 ppm. The monitored fluctuations are considered later on in the comparison with the numerical simulation.

Figure 3 shows corrected experimental data of the two in-situ sensors over time. The measured and temperature/pressure-corrected data of CO_2 concentration are then converted into x_{CO_2} in mol CO_2/mol water via Henry's law (Eq. (A4)) and $H_{aq,CO_2} = 9.37 \times 10^{-4}$ mol CO_2/ mol H_2O·atm in order to use this unit for the comparison with numerical simulations. At the start, both sensors for both corrections show a concentration of $x_{CO_2} \approx 0.4 \times 10^{-6}$ mol/mol, which corresponds well to an equilibrium with ambient air at $x_{CO_2} \approx 400$ ppm and 10 °C water temperature. After initiating the CO_2 influx into the head space, the first increase in CO_2 concentration can be observed almost simultaneously for both depths after $t \approx 10^5$ s. A peak in concentration appears after $t \approx 3 \times 10^5$ s, which seems to be an anomaly. This anomaly is mitigated in the

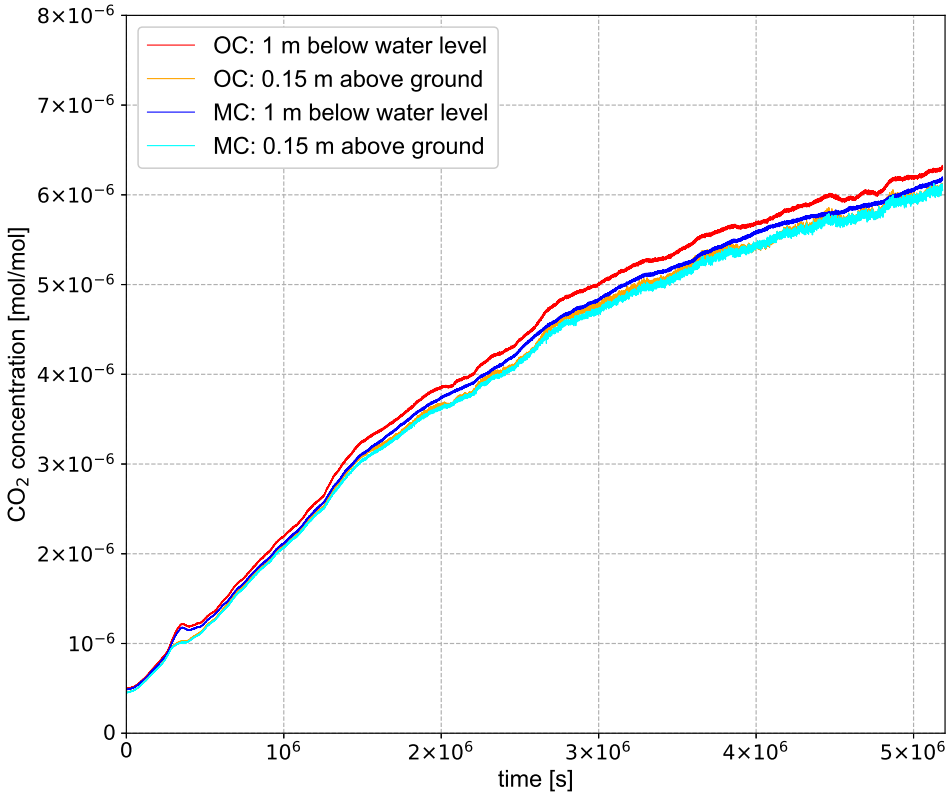

Figure 3. Corrected CO_2 concentration in the water column 1 m below water level and 0.15 m above ground, OC (own correction): red and orange are the concentrations corrected with the own compensation, MC (manufacturer correction): blue and light blue are the concentrations corrected with Eq. (1) as provided by the manufacturer.

second sensor and the question is whether or not this can be attributed to the density-induced fingering in the water column. It would make sense, but we cannot assess it with certainty. Beyond that, the concentration increases monotonously with time while the slope decreases with time. Stronger noise in the data can be seen in the second half of the plot for the deeper sensor. Also, both concentration signals are slightly drifting apart from each other over time. Beyond the time of 60 days, we expect that the curves further decrease in their slope until finally a state of equilibrium with the given CO_2 concentration at the water table in the head space is reached. Since the concentration difference is the driving force and gets smaller with time, this will go on for a longer period.

In Tab. 1, we provide parameters from an analysis of water samples from before and after 60 days. One may consider, e.g. the difference in total inorganic carbon (TIC), which is 4 mg/l. Using a molar mass of 12 g/mol for C and 44 g/mol for CO_2, this corresponds to 14.67 mg/l additional CO_2 in the later water sample. Converting this into added mole CO_2 per mole H_2O yields then about 6×10^{-6} mol/mol, which is in reasonable agreement with the values we see in Fig. 3. Alternatively, using the Bjerrum plot

and the measured pH-values, we could also estimate the CO_2 concentration from the TIC contents. At pH=8.16, there is only in the order of 1 % CO_2, while at pH=7.4 it approaches close to 10 % of the TIC. This would end up with about 4.6×10^{-7} mol/mol before the experiment and about 5.2×10^{-6} mol/mol after 60 days. Thus, we conclude that, although not being able to exactly figure measurement uncertainties, we have confidence that the observed CO_2 concentrations are reliable. In the next section, we describe the comparison with numerical simulations, where we use a model that does not consider water chemistry and pH, but only CO_2 dissolving according to Henry's law. Thus, the model does not account for the amount of newly dissolved CO_2 that transforms into HCO_3^-, which we estimate to be in this case in the order of 13 %, obtained from $\frac{6-5.2}{6}$, see the estimated numbers above. We should, thus, expect a slight overestimation of the predicted CO_2 concentrations.

2.3 Comparison with numerical simulations

Aiming primarily at better interpreting the experimental results, in this section here a modeling study compares experimental data to model results. In the model, the column is idealized as a 2D setup. In order to capture the effects that trigger the fingers at the top of the water body, a grid refinement in the upper parts is important for modelling the density-driven dissolution, see also (Class et al., 2020). It is important to resolve the formation of the layering due to CO_2-enriched water at the top and the resulting instability which then leads to fingering. In order to realize this, the topmost 50 cm of the model are graded vertically and discretized with 100 cells in vertical direction and 23 cells in horizontal direction, thus resulting in a minimum cell size at the top boundary of $\delta x = 0.0016$ m and $\delta z = 0.01$ m. For the remaining 5.05 m vertical length of the column, the mesh is regular with 505 cells in the vertical and 23 cells in the horizontal direction, thus resulting in this part in a discretization length of $\delta x = \delta z = 0.01$ m. The numerical model used for this study is the same isothermal model as in (Class et al., 2020). The model solves the continuity equations for the components water and CO_2, both present in the aqueous phase, as well as the Navier-Stokes equations. For details, we refer to Appendix A. As already mentioned before, the model neglects water chemistry and pH.

In the first instance, we ran two different realizations for the top boundary CO_2 concentration. In one realization, we assumed a constant CO_2 concentration at the top boundary, and, therefore, the mean concentration of the 60 days time period was used, i.e. $c_{CO2} = 20,707$ ppm in the column's head-space atmosphere. Using Henry's law, the dissolved CO_2 concentration can be calculated, and it is then implemented as Dirichlet boundary condition $x_{CO2} = 1.9498 \times 10^{-5}$ mol/mol at the top. In the second realization, an attempt was made to reproduce the fluctuations of CO_2 concentration as shown in Fig. 2. For this, the mean CO_2 concentration was calculated for ten-minutes intervals and tabulated. For each time step, the model can then take the associated mean value as the top boundary condition. Time-step size was limited to 10 minutes maximum, while, as controlled by the applied non-linear Newton solver and the corresponding convergence criteria (Koch et al., 2020), time steps were mostly between 60 s and 300 s. For comparing the simulations to the experimental data, the aqueous CO_2 concentration was read out in the simulation at the corresponding sensor locations.

Figure 4 shows the comparison of the measured and different realizations of simulated curves; the top chart shows the results for 1 m water depth and the bottom chart the results in 0.15 m from the bottom of the column. The blue and the red line (top) as well as the orange and the light blue line (bottom) represent the experimental data, thus the same as in Fig. 3. Green shows the simulation with constant CO_2 concentration at the top boundary and purple the one with the measured data in the column's head space. Grey and yellow represent non-isothermal simulations (shorter in time) and are discussed later on. The black line represents a realization with another Henry co-

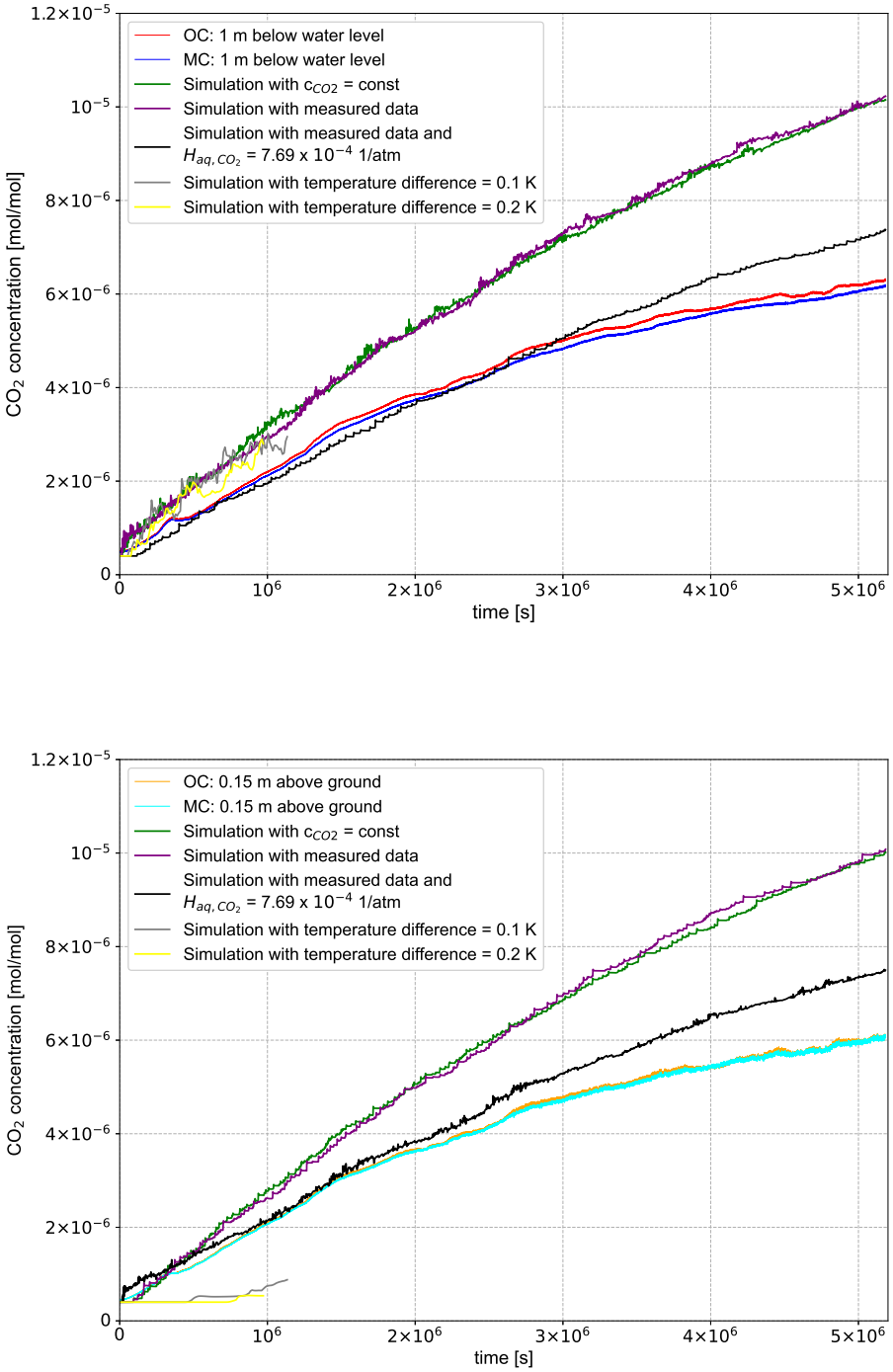

Figure 4. Comparison of experimental data with different realizations of numerical simulations; top figure shows curves in 1 m water depth, bottom figure in 0.15 m from the bottom. Please find detailed explanations in the text.

efficient applied to the gas-water interface and will be also discussed later on in this section. We see in Fig. 4 that simulations with constant CO_2 atmosphere (green) and with fluctuations like in the experiment (purple) do not show significant difference in the resulting overall aqueous CO_2 concentration as the two lines are almost on top of each other. The noise in the simulated curves is a result of the fingering, while the time delay in the sensor signal due to the required equilibration time prevents much of the resolution of these fluctuations in the measured curves. This is inherent to the measurement setup and not worrying. But it cannot be ignored that the simulations deviate from the experimental data systematically. There are different sources of error/uncertainty to explain this. We mentioned already above that we expect some overestimation in the order of 13 % since the water chemistry is neglected. This is clearly not sufficient to explain the observed difference. We believe that one major point could be due to a non-perfect cooling at the gas-water interface. As shown in Fig. 1, cooling and insulation did not include the lid, which holds around half of the column's air space. CO_2 was pumped into the lid at ambient temperature and cooled down only on its way to the water surface. If this path was not sufficient to cool the air to water temperature at the water table, then our assumption of the Henry coefficient to calculate how much CO_2 is dissolved is no longer correct. Gas solubility in liquids decreases with increasing temperature. To test this hypothesis, we have run one realization where we assumed a Henry coefficient corresponding to a higher temperature at the water table. Note that we did not attempt to calibrate the model, but we primarily aim at demonstrating the potential of this hypothesis to explain the observed deviation. We used a Henry coefficient of $H_{aq,CO_2} = 7.69 \times 10^{-4}$ mol CO_2/ mol H_2O·atm and with that obtained the black line in Fig. 4). This value corresponds to a temperature of $T = 16.8$ °C. Clearly, the black line shows much better agreement with the measurements in 1 m depth and still significantly better agreement in 5.40 m depth.

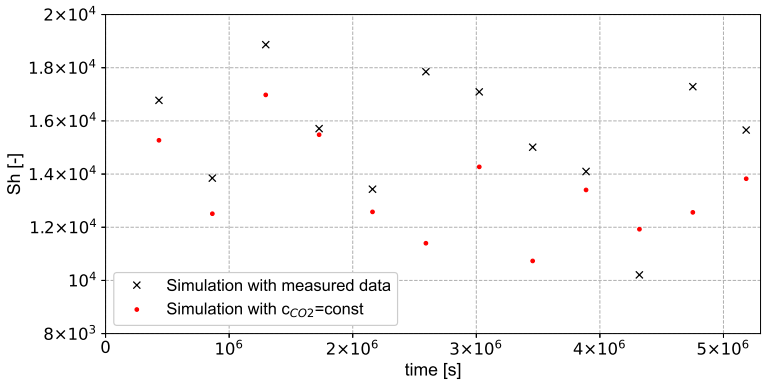

Figure 5. Sherwood numbers of the model realizations with measured CO_2 data and with c_{CO_2} = const. in the head space as top boundary condition, evaluated at time intervals of 5 days.

For an evaluation of the Sherwood number, see Eq. (2), we evaluated the influx of CO_2 at the top boundary as obtained from the numerical simulations. The result serves as an indicator for how large the actual CO_2 inflow is relative to a purely diffusive flow. It is shown in Fig. 5 at time intervals of 5 days. Whereas the influx of CO_2, in terms of $J_{in}^{CO_2}$, decreases over time due to a higher CO_2 concentration in the water and the associated smaller $\Delta\rho$, the Sherwood number seems to show no clear tendency, thereby underlying a zig-zag pattern at the evaluated points. The zig-zag pattern is due to the random nature of the vertically oriented fingering, which is not fully resolved in time in this plot. The fluctuations of $J_{in}^{CO_2}$ occur when convective fingers draw CO_2 downwards and

more CO_2 dissolves again at the water surface. In turn, this causes $J_{in}^{CO_2}$ to re-increase or to decrease while new fingers are just forming. The hypothetically assumed purely diffusive flux would scale solely with the concentration gradient. However, the concentration is also included in the Sherwood number via the $\Delta\rho$-values. Thus, we can infer that the influence of the density-driven flux relative to the purely diffusive flux does not lose significance as the experiment proceeds. The absolute CO_2 fluxes decrease over time, but the ratio of density-driven versus diffusive fluxes does not shift towards diffusive, because both the density gradient and the concentration gradient decrease.

Let us now scrutinize our assumption of isothermal conditions in the water column. Above, we already questioned this assumption for the very top of the water body, but does it hold inside the water column? Would it affect the fingering patterns if we had a deviation from isothermal conditions and would we be able to detect it?

In this case, we have to handle a double-diffusive problem, since temperature and CO_2 are both affected by diffusive processes, i.e. by diffusion and thermal conduction. To investigate the influence of temperature on the simulation results, we assumed a scenario in which the temperature stabilizes the system. This means, that warm and CO_2-rich water is located over colder water with less CO_2. This regime favors the formation of stable fingers in comparison with a single-diffusive problem without a temperature gradient, which predominantly forms convection cells (Kellner, 2016; Hage, 2010). The CO_2-rich, warm fluid sinks and, due to local instabilities, forms fingers that spread downwards. Due to the high thermal conductivity of water, the originally higher temperature within the fingers quickly equilibrates with the colder temperature in the surrounding. Since CO_2 diffuses much slower than heat due to small diffusion coefficients in the mixture with water, the concentration within the finger remains almost constant meanwhile. As a result, the finger is more stable and is able to spread further downwards. We performed two different non-isothermal simulations, in one case with a temperature difference of 0.1 K between top and bottom of the water body and of 0.2 K in the second case. For this, we added a thermal-energy balance equation to the numerical model. This significantly increases computational time, so we did not run the full period of 60 days, since we were able to draw the desired conclusions already much earlier. The results of the non-isothermal simulations are also shown as the grey and the yellow curves in Fig. 4, both shorter in time. It is clearly noticeable that both non-isothermal simulations, with a temperature gradient of 0.1 K and of 0.2 K, significantly underestimate the concentration of CO_2 compared to the experimental data and isothermal simulations at the same times. The formation of a stable fingering regime and the slow propagation velocity of fingers slows down the CO_2 transport within the column, resulting in a reduced concentration of CO_2 on the bottom of it. This can also be observed by looking at Fig. 6. The isothermal simulation on the left side forms convection cells which transport CO_2 quickly downwards. On the other hand, with increasing temperature gradient, more and more stable fingers are formed, which slows down the CO_2 transport. Furthermore, it can be observed that the higher difference of 0.2 K delivers an even lower concentration of CO_2 compared with the simulation with 0.1 K temperature difference. Based on these results, we are confident that effects of deviations from isothermal conditions within the water body do not play a major role in interpreting our observed data.

3 Generic scenario with background flow in a small laboratory flume

Using a generic lab-scale setup for a simulation study, we highlight now the role of background flow, in other words: forced convection, on the occurrence of distinct CO_2 fingering regimes. Recently, (Michel-Meyer et al., 2020) presented an experimentally supported study on the role of water flow and dispersion in density-driven dissolution related to geologic storage of CO_2. They concluded from their results that dissolution rates do not significantly decrease with increasing background flow even though fingering regimes are then getting suppressed. While the study of (Michel-Meyer et al., 2020) refers to pro-

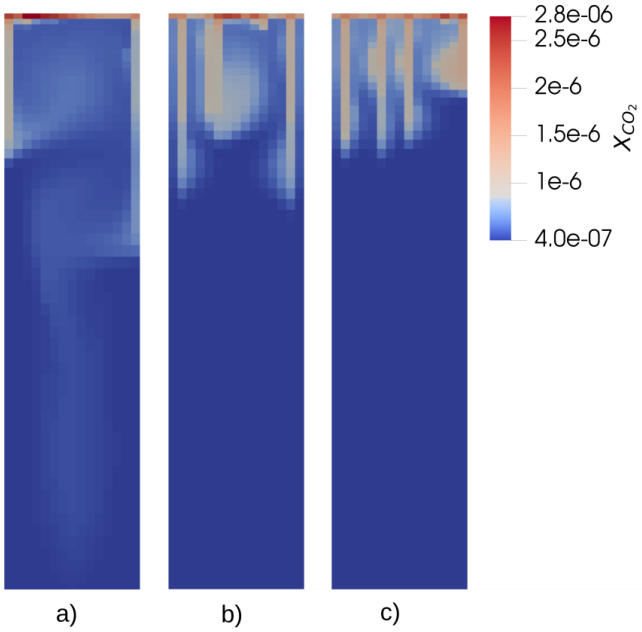

Figure 6. Comparison of finger flow between isothermal and non-isothermal simulation scenarios: a) isothermal, b) non-isothermal with 0.1 K temperature difference, c) non-isothermal with 0.2 K temperature difference.

cesses in porous media, we remind that our focus here is primarily on open water bodies, where we have no such experimental data available. The modeling study presented below builds on a small experimental laboratory setup, previously used by (Class et al., 2020) under stagnant conditions for validating the numerical Navier-Stokes model which is briefly explained in Appendix A.

3.1 Model setup and methods

The setup includes a water-filled flume, confined at the front and the back by two parallel glass plates with 1 cm distance in between. The flume is 57 cm wide and 32.5 cm high, see Fig. 7. (Class et al., 2020) applied different, but in each calculated scenario constant CO_2 partial pressures in the gas phase at the open top of the water-filled flume to trigger density-induced dissolution. We use the same isothermal numerical model as before, solving Navier-Stokes and continuity equations for water and CO_2, and again we refer to Appendix A. The model domain is discretized with a regular mesh, 54 cells in vertical and 95 cells in horizontal direction; thus, the discretization length is in both directions 0.006 m. The maximum time-step size is 30 s, which is in this case not limited by convergence criteria of the applied Newton solver.

As initial condition, the water in the flume has a very small concentration of dissolved CO_2, expressed by a mole fraction of $x_w^{CO2} = 2.5 \times 10^{-7}$. The boundary conditions are illustrated in Fig. 7. The bottom boundary and the upper parts (> 10 cm from the bottom) of the lateral boundaries are no-flow boundaries for water. An inflow velocity of water, v_N, with a constant dissolved CO_2 mole fraction of $x_{w,N}^{CO2} = 1.5 \times 10^{-5}$ is imposed at the lower part of the left lateral boundary, while the same amount of water flows out at the lower part of the right lateral boundary with the outflux of dissolved CO_2 being dependent on the local mole fractions x_w^{CO2}. The value of 1.5×10^{-5} was mea-

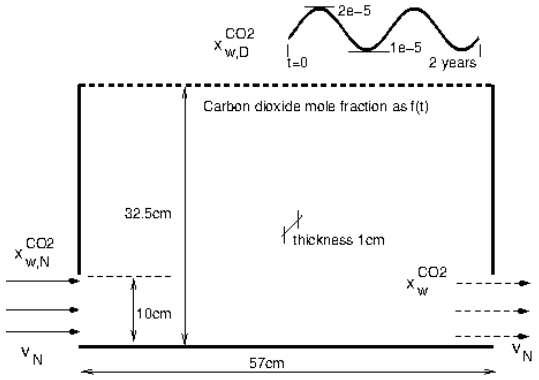

Figure 7. Schematic of the simulated scenario

sured by us on April 10 2021 in water collected in a karst cave (Laichinger Tiefenhöhle) on the Swabian Alb, a karstic mountain range in Southern Germany. At the top boundary, we imposed a seasonally varying CO_2 concentration $x_{w,D}^{CO2}$ as Dirichlet condition, with a sine-wave function that has $1{\times}10^{-5}$ and $2{\times}10^{-5}$ as its minimum and maximum values. We assume that this is in equilibrium with a gaseous CO_2 concentration at the water table. Applying this sinus curve is motivated from seasonal variations of biogenic CO_2. Thus, the CO_2 concentration at the influx, $x_{w,N}^{CO2}$ can be understood as a yearly averaged concentration. We consider this choice as adequate and reasonable for demonstrating the effects we intend to show with this generic setup. The plume thickness is 1 cm, and wall friction is considered accordingly by a thickness-dependent drag term in the Navier-Stokes equation, see Appendix A. Hence, the model solved in 2D can be viewed as a pseudo-3D approach. (Class et al., 2020) showed that this approach was able to reproduce experimental results in stagnant water satisfactorily.

We ran realizations of this numerical-modeling scenario with varying values for v_N and computed the CO_2 influx rate from the top boundary, J_{in}^{CO2}, as a model output. To evaluate this influx rate relative to the forced advective flow, we use the dimensionless Sherwood (Sh), Péclet (Pe), and Rayleigh (Ra) numbers. Sh was introduced before in Eq. (2) and relates the effective influx J_{in}^{CO2} to the purely diffusive flux rate. In this case here, we have $H = 0.325$ m (see Fig. 7), as the characteristic length scale. For $\Delta\varrho$, the characteristic density difference due to dissolved CO_2 concentrations, we employ here a calculation of water density at 8 °C according to Eq. (A5). With $x_{w,D}^{CO2} = 2 \times 10^{-5}$ and $x_{w,N}^{CO2} = 1.5 \times 10^{-5}$, this yields $\Delta\varrho = 2 \times 10^{-3}$ kg/m^3. Different than scenarios in geologic CO_2 sequestration where a plume of CO_2 segregated by gravitation rests on top of the brine, thus providing a constant value of dissolved concentration there, our study features a fluctuating CO_2 concentration to obtain the flux rate J_{in}^{CO2}. Therefore, choosing a characteristic value for $\Delta\varrho$ is not straightforward. We decided to evaluate these dimensionless numbers after $1{\times}10^7$ s, which is about the time when the maximum concentration is reached, see the results section further below.

Pe represents the ratio of advection versus diffusion, expressed here as

$$\mathrm{Pe} = \frac{v_N H}{D} \,, \tag{4}$$

and Ra is a measure for the instability, according to (Green & Ennis-King, 2018) given by

$$\mathrm{Ra} = \frac{k\, g\, \Delta\varrho\, H}{\mu\, D} \,. \tag{5}$$

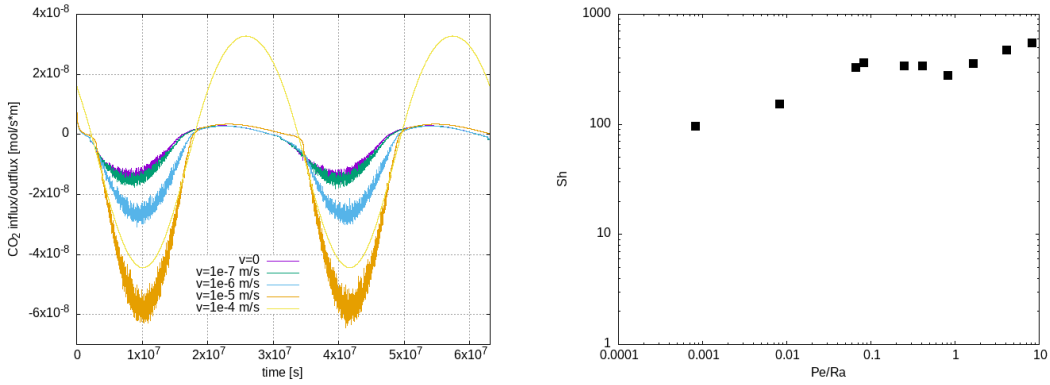

Figure 8. Left: CO_2 inflow (negative values) and outflow (positive) rate over two years at the top boundary of the flume, shown for scenarios with different in-/outflow velocities imposed at the bottom 10 cm of the lateral boundaries. Oscillatory curves indicate fingering regimes. Right: Mass influx evaluated at 10^7 s, expressed by Sh and plotted over Pe/Ra; note that not all points are represented as curves in the left plot.

g is the gravitational acceleration, μ the dynamic viscosity of water at 8 °C, $1.35{\times}10^{-}3$ kg/m s. Since this definition of Ra is taken from porous-media literature, k represents the permeability, which is approximated here as $k = b^2/12$ with thickness $b = 0.01$ m.

3.2 Results

Let us keep in mind our overall goal of substantiating the claim that density-driven dissolution of CO_2 is a relevant mechanism for replenishing karst waters. This directs our focus towards small background-flow velocities, so to speak gently forced convection, since at higher flow velocities the occurrence of fingering regimes is suppressed (Michel-Meyer et al., 2020). In analogy to studies related to thermal convection versus diffusion, we can distinguish the influence of natural convection due to density difference and forced convection by lateral flow. Fig. 8 (left) shows the total influx of CO_2 through the top boundary plotted over a time of two years for different lateral flow velocities v_N. Dividing this value by the length of the flume, we obtain the value of J_{in}^{CO2} as used in calculating the Sh number. It is evident that in periods where the CO_2 concentration at the top boundary is rising (see Fig. 7), the oscillatory behavior of the curves has to be attributed to fingering regimes. This corresponds to the phenomenon of natural convection, which is suppressed for larger values of v_N as the curve for $v_N = 1 \times 10^{-4}$ m/s clearly shows by its smoothness. The curves for smaller lateral velocities show that the influx during increasing CO_2 concentrations at the top boundary, i.e. during spring and summer seasons, is significantly higher than the outflux back to the atmosphere in winter periods. A cumulative net influx of CO_2 into the water over time is clearly obtained, which increases with the lateral flow velocity. In contrast, for lateral flow velocities above a critical threshold, where fingering regimes are suppressed, the dominant forced convection leads to a cumulative in-/outflux over time which is about zero. The CO_2 inflow is small for small v_N since the density difference diminishes when dissolved CO_2 is not removed by the lateral flow. There is obviously an optimum v_N, which is around 1×10^{-5} m/s for this particular setup.

Fig. 8 (right) plots the CO_2 inflow, expressed by the Sh number, over the ratio of Pe/Ra. A small Pe/Ra ratio corresponds to small v_N and, thus, to curves with small velocities in Fig. 8 (left). Note that the plot on the right contains points from simulations

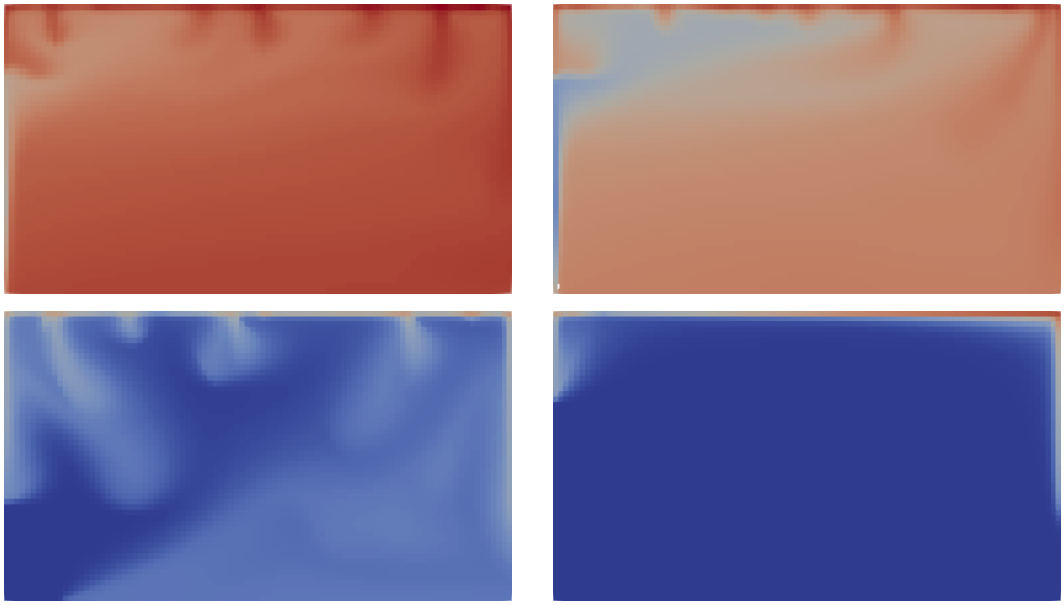

Figure 9. Plots of CO_2 mole fractions at 10^7 s for different background flow velocities, i.e. where CO_2 concentration at the top boundary is near its maximum.
From top left to bottom right: $v_N = 10^{-7}$ m/s, 10^{-6} m/s, 10^{-5} m/s, 10^{-4} m/s.
Legend: dark blue represents a value of 1.5×10^{-5}, dark red represents 1.95×10^{-5}.

which are not all shown in the left plot. We ran a few more simulations in the region around Pe/Ra≈1. As known from heat-convection studies, e.g., (Lai & Kulacki, 1991, 1990), there is a non-monotonic behavior of Sh for Pe/Ra with a local minimum around 1. For Pe/Ra>1, the forced-convection regimes dominate and mass transfer further increases. The local minimum at Pe/Ra≈1 is confirmed by the simulation results. Fingering regimes, our focus of interest, occur for Pe/Ra<1. The decrease of Sh for very small values of Pe/Ra is due to the accumulation of CO_2 in the water body, which is not sufficiently diluted by the smaller enforced lateral flow. Unlike in geologic CO_2 sequestration scenarios (Green & Ennis-King, 2018), we don't see here for small Pe/Ra ratios a steady flux regime for J_{in}^{CO2}. This has two reasons: first, the boundary condition ($x_{w,D}^{CO2}$) driving the fingering regime is not constant in time; second, the height of the setup is small here and for small Pe/Ra the CO_2 quickly accumulates in the flume and diminishes the density difference.

Fig. 9 displays plots of CO_2 mole fractions at $1{\times}10^7$ s, i.e. the time at which the dimensionless numbers were calculated above. The dark blue color corresponds to the value of $x_{w,N}^{CO2}$ (inflow concentration) and the dark red to the value of $x_{w,D}^{CO2}$ (maximum concentration at the top boundary). For v_N values of $1{\times}10^{-7}$ m/s, $1{\times}10^{-6}$ m/s, and $1{\times}10^{-5}$ m/s, fingering regimes can be easily recognized. For $v_N = 1{\times}10^{-4}$ m/s, there is no fingering regime anymore, only some minor effect of downward movement at the very left and very right of the domain in regions. With increasing v_N, the blue colors tend to dominate over the red. At small v_N, the blue color shows a vertically upward tendency which can be attributed to the density difference of the water. The low-concentrated water flowing in is lighter than the high-concentrated water and the forced convection is weak relative to this upward drive. This changes for higher v_N towards a domination of forced convection.

4 Discussion and outlook

The findings of this study may be classified on two different levels. On the one hand, we have provided experimental and numerical and, thus, quantified results on CO_2 dynamics in water exposed to well-defined concentrations of CO_2 in the gas phase above. On the other hand, we pursue an agenda of promoting a discussion on density-driven dissolution as a potentially relevant mechanism in karst systems in general. In fact, we are wondering why this did not get much attention so far, in particular since density-driven dissolution is known since many years as one of the major trapping mechanisms in geological storage of CO_2 (IPCC, 2005). Evidently, the CO_2 concentrations in caves and karst systems are much smaller than in geological storage. Thus, it requires quantification to evaluate the potential relevance of CO_2 density-driven dissolution for karst systems, which is what we provide with this study.

The design of our experimental setup in a stagnant water column allows for continuous and very accurate measurement of concentrations of dissolved CO_2 in different depths of the water body. The measured values are gas-phase concentrations, which were converted into dissolved concentrations via Henry's law. Starting at a very low concentration, $\approx$ 400 ppm - gas-phase equivalent-, and applying cave-like elevated CO_2 concentrations at the water table, $\approx$ 20,000 ppm (value confirmed by own measurement, similarly reported also by others, e.g. (Serrano-Ortiz et al., 2010)), we can quantify the CO_2 mass transfer into the water over time, which is crucially important to evaluate the potential impact of density-induced dissolution on the replenishment of the water with CO_2. Numerical simulations show very encouraging agreement with the experimental curves in spite of remaining uncertainties related to pressure-dependent correction of the sensor measurements and, in particular in our setup, probably a deviation from perfectly isothermal conditions at the air-water interface at the top of the column. An evaluation of dimensionless Sherwood numbers gives strong indication that the relative influence of density-driven transport of CO_2 versus purely diffusive transport is not strongly dependent on the concentration gradient of CO_2 in water. Even at small differences, density effects are dominating the influx rates of CO_2 at the gas-water interface. We consider this significant given the large time scales to be considered in karstification. The high measurement accuracy of the in-situ setup in the stagnant water column, that also (Johnson et al., 2010) claimed to achieve with a very similar Vaisala sensor setup, is here confirmed by the comparison with numerical simulations. This strengthens confidence that our model can capture the dynamics and, accordingly, it can be used to vary the experimental conditions to include the effect of background flow.

This was, in fact, done in the flume scenario, where, on the basis of the validation study of (Class et al., 2020), we introduced now in this study a forced convection, i.e. a background flow to compete with the natural convection due to density differences. There, we showed that, similar as in the recent study of (Tsinober et al., 2021), where a Darcy model was applied to CO_2 geological storage, our Navier-Stokes model applied to a seasonal cave-like scenario is able to capture the interaction between forced and natural convection. Results showed also here a local minimum of CO_2 mass transfer for a Pe/Ra ratio around 1. For Pe/Ra larger than 1, forced convection is dominant and density-driven dissolution does not play a major role anymore. Consequently, our interest is on the regimes with Pe/Ra smaller than 1. For very small background flow, mass-transfer rates are sooner or later leveling out since equilibrium between liquid concentration and gaseous concentration of CO_2 will be approached. This is what we see in the stagnant water column. The slope of the increasing CO_2 concentration in Fig. 3 is flattening over time. Therefore, in order to keep up the mass transfer of CO_2 from the gas phase into the water, a forced convective background flow is beneficial. The driving force for density-driven dissolution is determined by the present concentration in the water and by the concentration in the gas phase above the water table, i.e. in karst context: at the epiphreatic interface. Since we can imagine an enormous variability of hydrological conditions and sce-

narios, one may easily find therein scenarios where there are, for example, intermittent stagnant periods of water tables exposed to seasonally fluctuating CO_2 concentrations in the gas, interrupted by flow during and after infiltration events. For such situations, classical karstification theories do not mention a replenishment of CO_2 in the water during stagnant periods, while we clearly show that within a few months time, water concentrations of CO_2 can approach equilibrium conditions with cave-like CO_2 partial pressures at the water table.

The implications of this simple finding might have relevance beyond karst science and speleology. Let us, exemplarily, come back to (Ma et al., 2014), who wonder why "a downward CO_2 flux seems to have nowhere to go" and assume that fluctuations of groundwater levels carry dissolved inorganic carbon downward. Or to (Serrano-Ortiz et al., 2010) who postulate "hidden, abiotic CO_2 flows ... in the terrestrial carbon cycle". Is it possible that we have yet another mechanisms to add in explaining such seemingly mysterious phenomena? Although we put the focus of this study on karstification and, thus, on the water part of the overall processes at the interfaces between atmosphere, vadose zone, and phreatic zone, we expect that this topic may reach further into discussions of mass fluxes within carbon cycles, also relevant for climate models or for discussing options in mitigating climate change. It is worth noting that we did not yet thoroughly investigate the limits until when instabilities occur and, thus, density-driven dissolution plays a role. This may strongly depend on local hydrogeologic conditions, like heterogeneities, existence of pathways for air into open subterranean water bodies, availability of high permeable porous media that allow instabilities and significant mass transfer to occur, and also on temperature gradients, which can have stabilizing or destabilizing effects on density-driven dissolution of CO_2. We focused here first of all on karst systems, since there the existence of connected gas-flow paths reaching to karst-water tables is usually given, where triggering of fingering regimes due to instabilities is not limited by small permeabilities.

As an outlook, we plan to perform long-term measurements in a cave with seasonal fluctuations of CO_2 in the cave air and measure the dynamics of CO_2 concentrations in different water depths. In order to conclude on a potential contribution of density-driven CO_2 dissolution to speleogenesis, the kinetics of the reaction system with carbonates, CO_2, and water needs to be studied in relation to the transport mechanisms. Dissolution of carbonates has an additional effect on density and further changes the natural convection processes.

Appendix A Numerical model used in the simulations

A1 Governing equations

Continuity equation for each component $\kappa \in \{\mathrm{w},\mathrm{CO_2}\}$:

$$\frac{\partial\left(\varrho X^{\kappa}\right)}{\partial t} + \nabla\cdot\left(\varrho\mathbf{v}X^{\kappa} - D^{\kappa}\varrho\nabla X^{\kappa}\right) = 0\,. \tag{A1}$$

ϱ is the density of the aqueous phase, $\mathbf{v}$ is the velocity vector, D is the binary diffusion coefficient.

Navier-Stokes equation:

$$\frac{\partial(\varrho\mathbf{v})}{\partial t} + \nabla\cdot\left(\varrho\mathbf{v}\mathbf{v}^{\mathrm{T}}\right) = \nabla\cdot\left(\mu(\nabla\mathbf{v} + \nabla\mathbf{v}^{\mathrm{T}})\right) - \nabla p + \varrho\mathbf{g}\,. \tag{A2}$$

μ is the dynamic viscosity dependent on temperature, p is pressure, $\mathbf{g}$ is the gravitational acceleration vector.

The model is pseudo-3D. Assuming a parabolic velocity profile along the axis of the omitted dimension, a friction term is applied (Flekkøy et al., 1995):

$$\mathbf{f}_{\text{drag}} = -c\frac{\mu}{h^2}\mathbf{v} \ , \tag{A3}$$

which is added to the right-hand side of Eq. A2, with h the domain height in the neglected direction. $c = 12$ considers a height-averaged velocity.

The concentration of CO_2 at the interface between the atmosphere and the water body is calculated as a function of the partial pressure of CO_2 p_{CO_2} (in atm) in the ambient atmosphere by assuming equilibrium between the fluid phases. Accordingly, Henry's law is assumed to be valid:

$$x_{CO_2} = H_{aq,CO_2} p_{CO_2}, \tag{A4}$$

H_{aq,CO_2} (in mol CO_2/mol H_{20}·atm) is the temperature-dependent Henry constant for CO_2 in water.

A2 Numerical solution

The numerical simulator DuMu^x (`www.dumux.org`) provides the platform for solving the system of equations. All implementations that were used for this study can be reproduced and found for download at
`https://git.iws.uni-stuttgart.de/dumux-pub/buerkle2021a`.

We used for this study the *freeflow Navier-Stokes model* in DuMu^{x}and the *brineco2* fluid system.

Pressure, concentration (mole fraction) and the velocity vector are selected as primary unknowns for solving the system of equations with a staggered-grid method, that corresponds to a finite-volume method with different control volumes for different equations. The control volumes for the velocity components and the control volumes for the pressure and mass fractions are staggered. This provides a robust and mass conservative scheme without pressure oscillations. All equations are solved fully implicit in time using a Newton method to treat non-linearities. The Newton scheme adapts the time-step size to its convergence with a user-controlled maximum time-step size. For further details on discretization, numerical solution methods, and their implementation, we refer to (Koch et al., 2020) or the handbook of DuMu^x(Dumux handbook, n.d.).

A3 Density variation

The partial differential equations are coupled via the density which depends on the CO_2 concentration. We follow here an approach suggested by (Garcia, 2001).

The density (in kg/m^3) is computed as

$$\varrho = \frac{1}{x^{\mathrm{CO_2}} \frac{V_\phi}{M_T} + x^{\mathrm{H_2O}} \frac{M_{\mathrm{H_2O}}}{\varrho_w M_T}} \ . \tag{A5}$$

ϱ_w is the density of pure water dependent on pressure and temperature, $M_{\mathrm{H_2O}}$ is the molar mass (in kg/mol) of pure water, while M_T is accordingly obtained from

$$M_T = M_{\mathrm{H_2O}} x^{\mathrm{H_2O}} + M_{\mathrm{CO_2}} x^{\mathrm{CO_2}} \ . \tag{A6}$$

The apparent molar volume of dissolved CO_2 V_ϕ (in m^3/mol) is calculated as a function of temperature T (in °C) from

$$V_\phi = 1e^{-6}\,(37.51 - 9.585e^{-2}\,T + 8.74e^{-4}\,T^2 - 5.044e^{-7}\,T^3) \tag{A7}$$

Reference pure-water densities in this study were at 8 °C 999.85 kg/m^3 and at 20 °C 998.21 kg/m^3.

Appendix B Experimental methods

B1 Sensor compensation

Figure B1 shows the results of the sensor compensation explained in Sec. 2.1, CO_2 concentration plotted over overpressure.

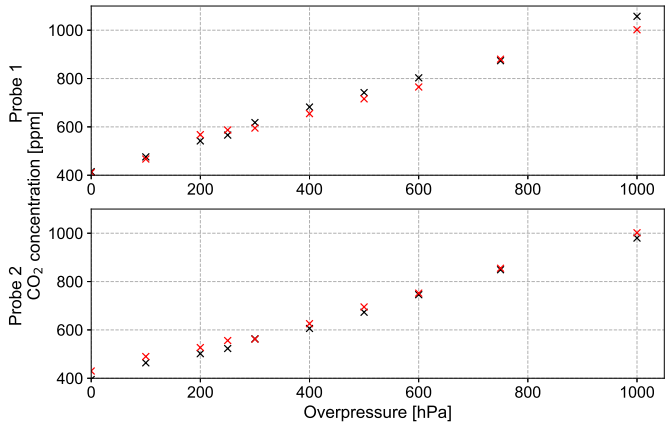

Figure B1. Compensation of the sensor probes, Probe 1 later installed at 1 m water depth and Probe 2 at 0.15 cm above ground.

Acknowledgments

The work is associated (without receiving funding) with Project C04 of the Collaborative Research Center 1313 (Project Number 327154368 – SFB 1313, German Research Foundation, DFG).

We thank Harald (Harry) Scherzer for providing inspiring ideas for this study. He is a geologist and a cave researcher and confronted us with his assumption of yet another mechanism with relevance for speleogenesis.

The datasets will be available in the Data Repository of the University of Stuttgart (DaRUS) (Bürkle et al., 2021). The datasets will be published along with the manuscript and are therefore not public yet. However, during the review process the datasets are accessible via the following url:

- `https://darus.uni-stuttgart.de/privateurl.xhtml?token=60539541-57d0-495f-a5d5-cd3a0707f8d2`

References

Atkinson, T. (1977). Carbon dioxide in the atmosphere of the unsaturated zone: an important control of groundwater hardness in limestones. *Journal of Hydrology*, *35*, 111-123. doi: 10.1016/0022-1694(77)90090-4

Audra, P., & Palmer, A. (2011). The pattern of caves: controls of epigenic speleogenesis. *Géomorphologie*, *17*(4), 359-378. doi: 10.4000/geomorphologie.9571

Bakalowicz, M. (2005). Karst groundwater: a challenge for new resources. *Hydrogeology Journal*, *13*, 148-160. doi: 10.1007/s10040-004-0402-9

Barrer, R., & Chio, H. (1965). Solution and diffusion of gases and vapours in silicone rubber membranes. *Journal of Polymer Science Part C: Polymer Symposia*, *10*, 111-138. doi: 10.1002/polc.5070100111

Bell, R., Short, R., van Amerom, F., & Byrne, R. (2007). Calibration of an in situ membrane inlet mass spectrometer for measurements of dissolved gases and volatile organics in seawater. *Environmental Science & Technology*, *41*(23), 8123-8128. doi: 10.1021/es070905d

Bénard, H. (1901). Les tourbillons cellulaires dans une nappe liquide. - Méthodes optiques d'observation et d'enregistrement. *J. Phys. Theor. Appl.*, *10*(1), 254-266. Retrieved from `https://hal.archives-ouvertes.fr/jpa-00240502` doi: 10.1051/jphystap:0190100100025400

Ben-Noah, I., & Friedman, S. (2018). Review and evaluation of root respiration and of natural and agricultural processes of soil aeration. *Vadose Zone Journal*, *17*, 170119. doi: 10.2136/vzj2017.06.0119

Berean, K., Ou, J. Z., Nour, M., Latham, K., McSweeney, C., Paull, D., ... Kalantar-zadeh, K. (2014). The effect of crosslinking temperature on the permeability of pdms membranes: Evidence of extraordinary CO_2 and CH_4 gas permeation. *Separation and Purification Technology*, *122*, 96-104. Retrieved from `https://www.sciencedirect.com/science/article/pii/S1383586613006503` doi: https://doi.org/10.1016/j.seppur.2013.11.006

Bögli, A. (1980). *Karst Hydrology and Physical Speleology.* Berlin Heidelberg: Springer.

Bonacci, O. (1987). *Karst Hydrology: With Special Reference to the Dinaric Karst.* Berlin Heidelberg: Springer.

Bürkle, P., Class, H., Zimmer, M., & Strauch, B. (2021). *Dataset of CO_2 dissolution longterm experiment.* `https://darus.uni-stuttgart.de/privateurl.xhtml?token=60539541-57d0-495f-a5d5-cd3a0707f8d2`.

Camilli, R., & Duryea, A. (2009). Characterizing spatial and temporal variability of dissolved gases in aquatic environments with in situ mass spectrometry. *Environmental Science & Technology*, *43*(13), 5014-5021. doi: 10.1021/es803717d

Cioni, R., Guidi, M., Pierotti, L., & Scozzari, A. (2007). An automatic monitoring network installed in Tuscany (Italy) for studying possible geochemical precursory phenomena. *Natural Hazards and Earth System Sciences*, *7*, 405-416. doi: 10.5194/nhess-7-405-2007

Class, H., Weishaupt, K., & Trötschler, O. (2020). Experimental and Simulation Study on Validating a Numerical Model for CO_2 Density-Driven Dissolution in Water. *Water*, *12*, 738.

De Gregorio, S., Camarda, M., Longo, M., Cappuzzo, S., Giudice, G., & Gurrieri, S. (2011). Long-term continuous monitoring of the dissolved CO2 performed by using a new device in groundwater of the Mt. Etna (southern Italy). *Water Research*, *45*(9), 3005-3011. doi: 10.1016/j.watres.2011.03.028

Dreybrodt, W. (1988). *Processes in Karst Systems - Physics, Chemistry, and Geology.* Berlin Heidelberg: Springer.

Dreybrodt, W. (2004). Dissolution: Carbonate rocks. *Encyclopedia of Caves and Karst Science*, 295-298.

DuMu^x handbook. (n.d.). `https://dumux.org/docs/handbook/master/dumux-handbook.pdf`. (Online; accessed 1-July-2021)

Emami-Meybodi, H., Hassanzadeh, H., Green, C., & Ennis-King, J. (2015). Convective dissolution of CO_2 in saline aquifers: Progress in modeling and experiments. *International Journal of Greenhouse Gas Control*, *40*, 238-266. doi: 10.1016/j.ijggc.2015.04.003

Ennis-King, J., & Paterson, L. (2003a). Rate of dissolution due to convective mixing in the underground storage of carbon dioxide. In J. Gale & Y. Kaya (Eds.), *Greenhouse gas control technologies* (Vol. 1, p. 507-510). Amsterdam, The Netherlands: Elsevier.

Ennis-King, J., & Paterson, L. (2003b). Role of convective mixing in the long-term storage of carbon dioxide in deep saline formations. In *Annual fall technical conference and exhibition, 5-8 october*. Denver, CO.

Erfani, H., Babaei, M., & Niasar, V. (2021). Dynamics of CO_2 density-driven flow in carbonate aquifers: effects of dispersion and geochemistry. *Water Resources Research*, *57*, e2020WR027829. doi: 10.1029/2020WR027829

Flekkøy, E. G., Oxaal, U., Feder, J., & Jøssang, T. (1995, November). Hydrodynamic dispersion at stagnation points: Simulations and experiments. *Physical Review E*, *52*(5), 4952–4962. Retrieved from `https://doi.org/10.1103/physreve.52.4952` doi: 10.1103/physreve.52.4952

Fohlmeister, J., Voarintsoa, N., Lechnleitner, F., Boyd, M., Brandtstätter, S., Jacobson, M., & Oster, J. (2020). Main controls on the stable carbon isotope composition of speleothems. *Geochimica et Cosmochimica Acta*, *279*, 67-87.

Ford, D., & Ewers, R. (1978). The development of limestone caves in the dimensions of length and depth. *International Journal of Speleology*, *10*, 213-244.

Ford, D., & Williams, P. (2007). *Karst Hydrogeology and Geomorphology*. Wiley.

Gabrovšek, F., & Dreybrodt, W. (2000). Role of mixing corrosion in calcite-aggressive H_2O-CO_2-$CaCO_3$ solutions in the early evolution of karst aquifers in limestone. *Water Resources Research*, *36*, 1179-1188. doi: 10.1029/1999WR900337

Garcia, J. (2001). *Density of Aqueous Solutions of CO_2* (Tech. Rep.). LBNL Report 49023, Lawrence Berkeley National Laboratory, Berkeley, CA, U.S.A.

Green, C., & Ennis-King, J. (2018). Steady flux regime during convective mixing in three-dimensional heterogeneous porous media. *Fluids*, *3*(58), 1-21. doi: 10.3390/fluids3030058

Gulley, J., Martin, J., & Moore, P. (2014). Vadose CO_2 gas drives dissolution at water tables in eogenetic karst aquifers more than mixing dissolution. *Earth Surface Processes and Landforms*, *39*, 1833-1846. doi: 10.1002/esp.3571

Hage, E.-C. (2010). *Experimentelle Untersuchungen doppelt diffusiver Konvektion im Finger-Regime* (Doctoral dissertation, Georg-August-Universität Göttingen). Retrieved from `https://ediss.uni-goettingen.de/bitstream/handle/11858/00-1735-0000-0006-B4CD-D/hage.pdf?sequence=1`

Hassanzadeh, H., Pooladi-Darvish, M., & Keith, D. (2005). Modelling of convective mixing in CO_2 storage. *Journal of Canadian Petroleum Technology*, *44*(10). doi: 10.2118/05-10-04

Hassanzadeh, H., Pooladi-Darvish, M., & Keith, D. (2006). Stability of a fluid in a horizontal saturated porous layer: effect of non-linear concentration profile, initial, and boundary conditions. *Transport in Porous Media*, *65*(2), 193-211. doi: 10.1007/s11242-005-6088-1

Hassanzadeh, H., Pooladi-Darvish, M., & Keith, D. (2007). Scaling behavior of convective mixing, with application to geological storage of CO_2. *American Institute of Chemical Engineers Journal*, *53*, 1121-1131. doi: 10.1002/aic.11157

Houillon, N., Lastennet, R., Denis, A., & Malaurent, P. (2020). The CO_2 Dynamics in the Continuum Atmosphere-Soil-Epikarst and Its Impact on the Karstification Potential of Water: A Case Study of the Lasceaux Cave Site (Montignac, France). In C. Bertrand, S. Denimal, M. Steinmann, & P. Renard (Eds.), *Eurokarst 2018, Besancon - Advances in the Hydrogeology of Karst and*

Carbonate Reservoirs (p. 93-99). Springer Nature Switzerland.

IPCC. (2005). *Special report on carbon dioxide capture and storage* (Tech. Rep.). Cambridge University Press, Cambridge, United Kingdom and New York, NY, USA: Intergovernmental Panel on Climate Change (IPCC), prepared by Working Group III (Metz, B., O. Davidson, H.C. de Conink, M. Loos and L.A. Meyer (eds)). Retrieved from `https://www.ipcc.ch/site/assets/uploads/2018/03/srccs_wholereport-1.pdf`

Javaid, A. (2005). Membranes for solubility-based gas separation applications. *Chemical Engineering Journal*, *112*(1-3), 219-226. doi: 10.1016/j.cej.2005.07.010

Johnson, M., Billett, M., Dinsmore, K., Wallin, M., Dyson, K., & Jassal, R. (2010). Direct and continuous measurement of dissolved carbon dioxide in freshwater aquatic systems method and applications. *Ecohydrology*, *3*(1), 68-78. doi: 10.1002/eco.95

Kana, T., Darkangelo, C., Hunt, M., Oldham, J., Bennett, G., & Cornwell, J. (1994). Membrane inlet mass spectrometer for rapid high-precision determination of N_2, O_2, and Ar in environmental water samples. *Analytical Chemistry*, *66*(23), 4166-4170. doi: 10.1021/ac00095a009

Kaufmann, G., Gabrovšek, F., & Romanov, D. (2014). Deep conduit flow in karst aquifers revisited. *Water Resources Research*, *50*, 4821-4836. doi: 10.1002/2014WR015314

Kellner, M. (2016). Experimentelle untersuchungen von fingerströmung und thermohalinen treppen für instabile auftriebsverhältnisse.

Kjeldsen, P. (1993). Evaluation of gas diffusion through plastic materials used in experimental and sampling equipment. *Water Research*, *27*(1), 121-131. doi: 10.1016/0043-1354(93)90202-S

Klimchouk, A., Ford, D., Palmer, A., & Dreybrodt, W. (Eds.). (2000). *Speleogenesis - Evolution of Karst Aquifers*. Huntsville Alabama: National Speleological Society.

Kluge, F. (2012). *Kluge Etymologisches Wörterbuch der Deutschen Sprache* (25th ed.; E. Seebold, Ed.). Berlin Heidelberg: De Gruyter.

Koch, T., Gläser, D., Weishaupt, K., Ackermann, S., Beck, M., Becker, B., ... Flemisch, B. (2020). DuMu^x 3 – an open-source simulator for solving flow and transport problems in porous media with a focus on model coupling. *Computers & Mathematics with Applications*. doi: 10.1016/j.camwa.2020.02.012

Kukuljan, L., Gabrovšek, F., Covington, M., & Johnston, V. (2021). CO_2 dynamics and heterogeneity in a cave atmosphere: role of ventilation patterns and airflow pathways. *Preprint*. doi: 10.13140/RG.2.2.17204.17284

Lai, F., & Kulacki, F. (1990). The influence of lateral mass flux on mixed convection over inclined surfaces in saturated porous media. *Journal of Heat Transfer*, *112*(2), 515-518. doi: 10.1115/1.2910414

Lai, F., & Kulacki, F. (1991). Experimental study of free and mixed convection in horizontal porous layers locally heated from below. *International Journal of Heat and Mass Transfer*, *34*(2), 525-541. doi: 10.1016/0017-9310(91)90271-F

Lee, K. Y., van Geldern, R., & Bart, J. A. (2021). Extreme gradients in CO_2 losses downstream of karstic springs. *Science of the Total Environment*, *778*, 146099. doi: 10.1016/j.scitotenv.2021.146099

Lindeberg, E., & Wessel-Berg, D. (1997). Reservoir storage and containment of greenhouse gases. *Transport in Porous Media*, *38*, S229-S234. doi: 10.1016/s0196-8904(96)00274-9

Lord Rayleigh, O. F. (1916). Lix. on convection currents in a horizontal layer of fluid, when the higher temperature is on the under side. *The London, Edinburgh, and Dublin Philosophical Magazine and Journal of Science*, *32*(192), 529-546. Retrieved from `https://doi.org/10.1080/14786441608635602` doi: 10.1080/14786441608635602

Ma, J., Lio, R., Tsang, L.-S., Lan, Z.-D., & Li, Y. (2014). A downward CO_2 flux seems to have nowhere to go. *Biogeosciences*, *11*, 6251-6262. doi: 10.5194/bg-11-6251-2014

Mangin, A. (1975). *Contribution à l'étude hydrodynamique des aquifères karstiques* (Doctoral dissertation, Université de Dijon, Sciences de la Terre). Retrieved from `https://hal.archives-ouvertes.fr/tel-01575806`

Merkel, T., Bondar, V., Nagai, K., Freeman, B., & Pinnau, I. (2000). Gas sorption, diffusion, and permeation in poly(dimethylsiloxane). *Journal of Polymer Science: Part B: Polymer Physics*, *38*, 415-434. doi: 10.1002/(SICI)1099-0488(20000201)38:3⟨415::AID-POLB8⟩3.0.CO;2-Z

Michel-Meyer, I., Shavit, U., Tsinober, A., & Rosenzweig, R. (2020). The Role of Water Flow and Dispersive Fluxes in the Dissolution of CO_2 in Deep Saline Aquifers . *Water Resources Research*, *56*(11), e2020WR028184. doi: 10.1029/2020WR028184

Mohammadi, Z., Raeisi, E., & Bakalowicz, M. (2007). Method of leakage study at the karst dam site. A case study: Khersan 3 Dam, Iran. *Environmental Geology*, *52*, 1053-1065. doi: 10.1007/s00254-006-0545-1

Pau, G., Bell, J., Pruess, K., Almgren, A., Lijewski, M., & Zhang, K. (2010). High resolution simulation and characterization of density-driven flow in CO_2 storage in saline aquifers. *Advances in Water Resources*, *33*, 443-455.

Peyraube, N., Lastennet, R., Denis, A., Malaurent, P., & Villanueva, J. (2015). Interpreting CO_2-SIc relationship to estimate CO_2 baseline in limestone aquifers. *Environmental Earth Sciences*, *1*, 19-26. doi: 10.1007/s12665-014-3316-4

Pfeiffer, T. J., Summerfelt, S. T., & Watten, B. J. (2011). Comparative performance of CO_2 measuring methods: Marine aquaculture recirculation system application. *Aquacultural Engineering*, *44*(1), 1-9. Retrieved from `https://www.sciencedirect.com/science/article/pii/S0144860910000683` doi: https://doi.org/10.1016/j.aquaeng.2010.10.001

Pinnau, I., & He, Z. (2004). Pure and mixed gas permeation properties of polydimethylsiloxane for hydrocarbon/methane and hydrocarbon/hydrogen separation. *Journal of Membrane Science*, *244*(1-2), 227-233. doi: 10.1016/j.memsci.2004.06.055

Raharjo, R., Freemann, B., Paul, D., Sarti, G., & Sanders, E. (2007). Pure and mixed gas CH_4 and n-C_4H_{10} permeability and diffusivity in poly(dimethylsiloxane). *Journal of Membrane Science*, *306*(1-2), 75-92. doi: 10.1016/j.memsci.2007.08.014

Riaz, A., Hesse, M., Tchelepi, H., & Orr, F. (2006). Onset of convection in a gravitationally unstable diffusive boundary layer in porous media. *Journal of Fluid Mechanics*, *548*, 87-111. doi: 10.1017/S0022112005007494

Scholes, C., Kentish, S., & Stevens, G. (2009). The effect of condensable minor components on the gas separation performance of polymeric membranes for carbon dioxide capture. *Energy Procedia*, *1*, 311-317. doi: 10.1016/j.egypro.2009.01.043

Schultz, J., & Peinemann, K. (1996). Membranes for separation of higher hydrocarbons from methane. *Journal of Membrane Science*, *110*(1), 37-45. doi: 10.1016/0376-7388(95)00214-6

Serrano-Ortiz, P., Roland, M., Sanchez-Moral, S., Janssens, I., Domingo, F., Goddéris, Y., & Kowalsko, A. (2010). Hidden, abiotic CO_2 flows and gaseous reservoirs in the terrestrial carbon cycle: Review and perspectives. *Agricultural and Forest Meteorology*, *150*, 321-329. doi: 10.1016/j.agrformet.2010.01.002

Spötl, C., Desch, A., Dublyansky, Y., Plan, L., & Mangini, A. (2016). Hypogene speleogenesis in dolimite host rock by CO_2-rich fluids, Kozak Cave (southern Austria). *Geomorphology*, *255*, 39-48.

Stern, S., Shah, V., & Hardy, B. (1987). Structure-permeability relationships in silicone Polymers. *Journal of Polymer Science: Part B: Polymer Physics*, *25*,

1263-1298. doi: 10.1002/polb.1987.090250607

Stevanovic, Z. (2015). *Karst Aquifers - Characterization and Engineering.* Cham Heidelberg New York Dordrecht London: Springer.

Strauch, B., Heeschen, K. U., Schicks, J. M., Spangenberg, E., & Zimmer, M. (2020). Application of tubular silicone (PDMS) membranes for gas monitoring in CO_2–CH_4 hydrate exchange experiments. *Marine and Petroleum Geology*, *122*, 104677. doi: https://doi.org/10.1016/j.marpetgeo.2020.104677

Tsinober, A., Rosenzweig, R., Class, H., Helmig, R., & Shavit, U. (2021). The role of forced convection, natural convection, and hydrodynamic dispersion during CO_2 dissolution in saline aquifers. *Water Resources Research*. (submitted, currently implementing major revisions)

Weir, G. J., White, S. P., & Kissling, W. M. (1996). Vertical convection in an aquifer column under a gas cap of CO_2. *Energy Conversion and Management*, *23*, 37-60. doi: 10.1007/BF00145265

Werth, M., & Kuzyakov, Y. (2010). 13C fractionation at the root-microorganisms-soil interface: A review and outlook for partitioning studies. *Soil Biology and Biochemistry*, *43*(9), 1372-1384. doi: 10.1016/j.soilbio.2010.04.009

White, W. (2018). *Caves and Karst of the Greenbrier Valley in West Virginia.* Cham: Springer.

Zimmer, M., Erzinger, J., Kujawa, C., & CO2-SINK-Group. (2011). The gas membrane sensor (GMS): a new method for gas measurements in deep boreholes applied at the CO2 SINK site. *International Journal of Greenhouse Gas Control*, *5*, 995-1001. doi: 10.1016/j.ijggc.2010.11.007